nature communications

Article

https://doi.org/10.1038/s41467-024-54353-4

Absence of MCJ/DnaJC15 promotes brown adipose tissue thermogenesis

Received: 10 March 2024

Accepted: 6 November 2024

Published online: 13 January 2025

Check for updates

Beatriz Cicuéndez[1,2], Alfonso Mora[1,2], Juan Antonio López[1,3], Andrea Curtabbi[1,4], Javier Pérez-García[2], Begoña Porteiro[5,6], Daniel Jimenez-Blasco[4,7,8], Pedro Latorre-Muro[9,10], Paula Vo[11], Madison Jerome[11], Beatriz Gómez-Santos[12], Rafael Romero-Becerra[1], Magdalena Leiva[13], Elena Rodríguez[1,2], Marta León[1,2], Luis Leiva-Vega[1,2], Noemi Gómez-Lado[14,15,16], Jorge L. Torres[17], Lourdes Hernández-Cosido[18], Pablo Aguiar[14,15,16], Miguel Marcos[19,20], Martin Jastroch[21], Andreas Daiber[22,23], Patricia Aspichueta[12,24], Juan Pedro Bolaños[4,7,8], Jessica B. Spinelli[11,25], Pere Puigserver[9,10], José Antonio Enriquez[1,4], Jesús Vázquez[1,3], Cintia Folgueira[1,2,6] ✉ & Guadalupe Sabio[1,2] ✉

Obesity poses a global health challenge, demanding a deeper understanding of adipose tissue (AT) and its mitochondria. This study describes the role of the mitochondrial protein Methylation-controlled J protein (MCJ/DnaJC15) in orchestrating brown adipose tissue (BAT) thermogenesis. Here we show how MCJ expression decreases during obesity, as evident in human and mouse adipose tissue samples. MCJ^{KO} mice, even without UCP1, a fundamental thermogenic protein, exhibit elevated BAT thermogenesis. Electron microscopy unveils changes in mitochondrial morphology resembling BAT activation. Proteomic analysis confirms these findings and suggests involvement of the eIF2α mediated stress response. The pivotal role of eIF2α is scrutinized by in vivo CRISPR deletion of eIF2α in MCJ^{KO} mice, abrogating thermogenesis. These findings uncover the importance of MCJ as a regulator of BAT thermogenesis, presenting it as a promising target for obesity therapy.

Obesity is a global health problem affecting 650 million people worldwide and represents an important predisposing factor for cardiometabolic diseases[1,2]. Despite the societal impact of obesity, understanding the molecular mechanisms and multiple factors through which obesity leads to disease is still limited. In this multi-organ framework, adipose tissue (AT), the main fat-storage organ, is critical for energy homeostasis[3,4]. Although fat-storage was considered the only function of AT for many years, it is now recognized as a complex and multi-faceted organ. AT is an essential and highly active regulator of whole-body metabolism, providing mechanical protection, thermal insulation, and energy storage; and mediating immune responses, endocrine functions, as well as non-shivering thermogenesis[5]. Current knowledge positions AT as a central rheostat in the regulation of systemic nutrient and energy homeostasis[6]. In fact, AT is key to the control of whole-body metabolism[7] and thus, modulating its function likely protects against obesity[8–10].

While white adipose tissue (WAT) stores energy in the form of triglycerides and releases free fatty acids on demand, BAT is responsible for thermogenesis, playing a central role in maintaining body temperature by burning fat upon activation in response to cold or other stimuli[11]. Non-shivering thermogenesis in BAT is mediated primarily by uncoupling protein 1 (UCP1). This protein uncouples substrate oxidation from ATP production, leading to increased heat generation[12]. Recent studies suggest that UCP1-independent mechanisms including other regulators of mitochondrial function are also important for the regulation of thermogenesis[13,14]. Ambient temperature significantly influences the outcomes of metabolic experiments, given the necessity for mammals to thermoregulate. Adaptive

A full list of affiliations appears at the end of the paper. ✉e-mail: cintia.folgueira@cnic.es; gsabio@cnio.es

thermogenesis is activated when extra heat is required to defend body temperature below thermoneutrality. Classical, adaptive non-shivering thermogenesis is primarily attributed to BAT activity, and long-term adaptation to the cold recruits more BAT to increase capacity[15].

Mitochondria are key organelles in adipocyte metabolism, controlling ATP production, energy expenditure and ROS disposal. Adequate mitochondrial function is needed to maintain an appropriate balance between energy storage and expenditure. Alterations of mitochondrial physiology are observed during obesity to adapt functionally to the new energy demands[16]. Obesity and metabolic diseases have been linked to mitochondrial dysfunction in AT both in mouse models and human patients[17]; where incorrect mitochondrial adaptation may trigger type 2 diabetes, insulin resistance, and aging[17,18]. A better understanding of how adipose mitochondria function is fine-tuned mechanistically in response to diverse external stimuli can lead to the development of promising therapeutic approaches to combat obesity and its comorbidities.

Methylation-controlled J protein (MCJ/DnaJC15) is a transmembrane protein located in the mitochondrial inner membrane known to be an inhibitor of respiratory chain complex I[19]. This protein has been previously implicated in the adaptation of hepatocytes to fasting[19]. MCJ/DnaJC15 deletion in hepatocytes protects animals against steatosis and from the development of fibrosis under western and methionine choline deficient diet (MCD)[20], as well as alcohol-associated liver disease[21].

Here, we discovered that BAT activation is modulated by the mitochondrial protein MCJ/DnaJC15, whose expression is decreased in humans and mice during obesity. Our investigation sheds light on the role of MCJ/DnaJC15 in BAT and its significance in the context of obesity, contrasting previous research that has extensively explored MCJ/DnaJC15's impact on liver function and its protective role against liver steatosis[20]. MCJ/DnaJC15 plays a pivotal role in regulating AT thermogenesis and BAT-specific deletion not only enhances thermogenic capacity but also decreases body weight. These results provide evidence for the potential therapeutic implications of MCJ/DnaJC15 modulation in combating obesity, offering fresh avenues for the intervention of this critical health issue.

Results

Reduced MCJ expression in human adipose tissue during obesity

To evaluate the possible role of MCJ in adipose tissue, we investigated MCJ levels in human subcutaneous WAT (WATsc) during obesity, when AT thermogenesis is reduced[22–24]. Our cohort of 135 adult patients revealed a reduction of MCJ expression in WATsc from individuals with obesity compared to control subjects (Fig. 1A). Notably, mRNA levels of *DNAJC15* exhibited an inverse correlation with both body fat percentage and body mass index (BMI) (Supplementary Fig. 1A). In parallel, mice fed a high-fat diet (HFD) also displayed decreased MCJ expression in both WATsc and BAT (Fig. 1B). Interestingly cold exposure also reduced MCJ levels in BAT (Supplementary Fig. 1B). This indicates that MCJ may be downregulated by both thermal and dietary challenges to enhance thermogenesis. Collectively, these findings point to a potential role of MCJ in regulating adipose tissue adaptation to obesity in both humans and mice.

The absence of MCJ protects against obesity and increases interscapular temperature

To elucidate the role of MCJ in controlling metabolism during obesity, we conducted an experiment involving MCJ^{KO} and WT mice. We subjected these mice to either a chow diet (CD) or a high-fat diet (HFD) for 8 weeks (Fig. 1C). Under CD conditions, we observed no significant differences in body weight or various metabolic parameters, including body composition, energy expenditure, respiratory quotient, food intake, locomotor activity, and BAT temperature between the two groups (Fig. 1D–I and Supplementary Fig. 1C–E).

However, when exposed to HFD, MCJ^{KO} mice showed outcomes distinct from WT control mice. MCJ^{KO} mice displayed less weight gain (Fig. 1E) and fat mass accumulation (Fig. 1F), with no discernible alterations in lean mass (Fig. 1G). This coincided with an increased energy expenditure (Fig. 1H), demonstrated by indirect calorimetry. While this increase did not correspond to changes in respiratory quotient or food intake (Supplementary Fig. 1C, D), BAT temperature was significantly increased in MCJ^{KO} mice under HFD conditions (Fig. 1I). In contrast, there were no notable differences in ambulatory and vertical movement between the two genotypes (Supplementary Fig. 1E). To delve deeper into MCJ's role in BAT metabolism, we conducted an analysis of BAT morphology in MCJ^{KO} and WT mice. While no differences in BAT histology were noticed under CD, we observed that the increased accumulation of lipid droplets after HFD feeding was prevented in MCJ^{KO} mice (Fig. 1J).

To evaluate the role of BAT thermogenesis for the protection against obesity, we maintained the mice at thermoneutrality to reduce thermogenic response. In agreement with the protection mediated by BAT thermogenesis we found that HFD fed MCJ^{KO} mice at 30 °C displayed the same body weight during HFD, BAT temperature and BAT morphology as their wildtype counterparts (Supplementary Fig. 1F–I).

Enhanced BAT temperature and obesity protection through BAT-specific MCJ deficiency in adipocytes

To investigate the specific role of MCJ in BAT, we employed an adeno-associated virus (AAV) carrying an MCJ-targeting shRNA, which was expressed under the adipocyte-specific aP2 mini promoter (pAAV-miniaP2mir122-EGFP-shMCJ)[8] and a multiple repetition of miR122 target to avoid expression in other type of cells[25]. Additionally, a control mini aP2 mir122 scramble vector plasmid was used as control (pAAV-miniaP2mir122-EGFP-shscramble) (Fig. 2A). These constructions were administered directly into the BAT of WT mice. MCJ protein levels were reduced in BAT as confirmed by Western-blot (Fig. 2B) and qRT-PCR analysis (Fig. 2C). To clarify whether the MCJ reduction was specific to brown adipocytes, we performed qRT-PCR analysis on fractionated adipose tissue. We detected that MCJ inhibition occurs specifically in the brown adipocyte fraction, while no alteration in MCJ levels was observed in the stromal vascular fraction (SVF), demonstrating that the deletion is specific to adipocytes (Fig. 2D). We further evaluated the consequences of the viral infection by analyzing BAT inflammation in comparison with non-infected wild-type mice. None of the infected groups showed any changes either in macrophages infiltration (Supplementary Fig. 2A–C) or in interleukin levels (Supplementary Fig. 2D) in the BAT. Therefore, we conclude that administering AAV in the BAT does not lead to an inflammatory response to which would impact affect our study's functionality. This specific downregulation of MCJ in adipocytes resulted in an increase of BAT temperature (Fig. 2E).

We performed glucose and insulin tolerance tests in our shMCJ BAT HFD mice and checked fasting blood glucose levels. We observed that in fasting conditions, HFD-fed shMCJ BAT mice present lower glucose levels compared with control mice (Fig. 2F), as well as improved glucose tolerance and insulin sensitivity (Fig. 2G, H). Furthermore, we observed that the reduction of MCJ in BAT imposes beneficial metabolic effects by decreasing triglyceride levels, low density lipoprotein (LDL) and high-density lipoprotein (HDL) cholesterol, as well as total cholesterol and non-esterified fatty acids (NEFA) levels (Fig. 2I–M). This indicates that the absence of MCJ in BAT not only improves obesity by increasing thermogenesis but also improves the plasma lipid profile and enhances glucose and insulin tolerance on HFD.

To further evaluate the function of MCJ in BAT, we conducted interscapular BAT transplantation, following established protocols[26,27]. Specifically, after 3 weeks of exposure to HFD we transplanted WT mice with BAT from MCJ^{KO} or WT mice (Fig. 2N). The transplanted BAT exhibited a normal appearance, as previously

https://doi.org/10.1038/s41467-024-54353-4

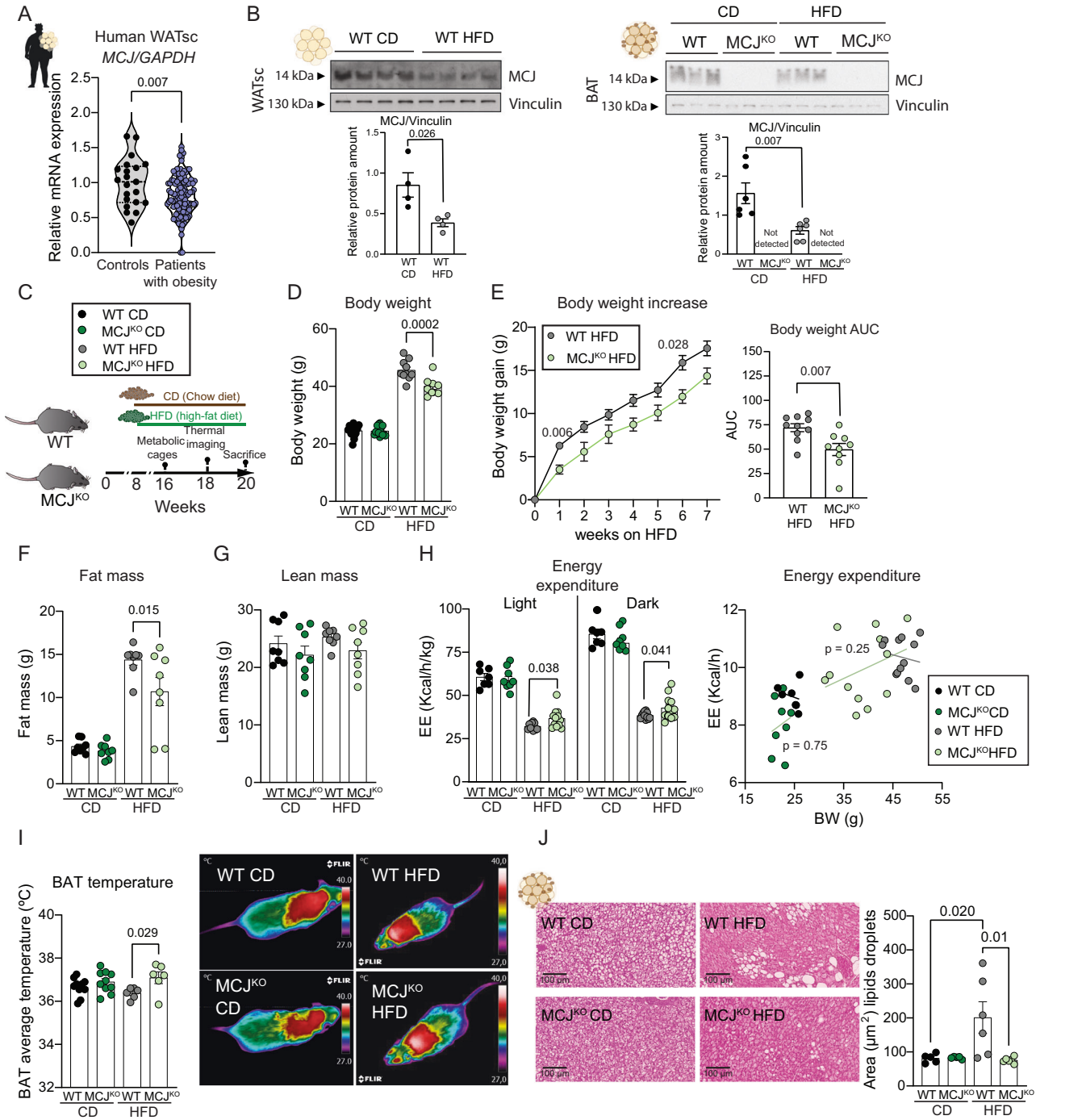

Fig. 1 | The absence of MCJ protects against obesity increasing interscapular temperature while not affecting the metabolism on chow diet. A mRNA levels of MCJ in subcutaneous fat from lean individuals ($n = 21$) and patients with obesity ($n = 114$). mRNA expression was normalized to the amount of *GAPDH* mRNA. **B** Representative immunoblot analysis showing MCJ expression in WATsc (WT CD and HFD $n = 4$) and BAT lysate (WT and MCJ^{KO} CD and HFD $n = 6$) from WT or MCJ^{KO} CD and HFD-fed mice for 12 weeks. Vinculin protein expression was monitored as a loading control. **C** WT and MCJ^{KO} male (8 wk-old) mice were HFD-fed or CD-fed for 12 weeks and metabolic parameters were assayed. **D** Body weight at the end of diet (WT CD and MCJ^{KO} CD $n = 15$; WT HFD $n = 10$, MCJ^{KO} HFD $n = 9$); (**E**) body weight time course and area under the curve over 8 weeks (WT $n = 10$; MCJ^{KO} $n = 9$), (**F**) fat mass (WT CD, MCJ^{KO} CD, WT HFD and MCJ^{KO} HFD $n = 8$), (**G**) lean mass (WT CD, MCJ^{KO} CD, WT HFD and MCJ^{KO} HFD $n = 8$), (**H**) energy expenditure (EE) corrected by BW and respect to BW over 2-days (WT CD $n = 7$; MCJ^{KO} CD $n = 8$; WT HFD and MCJ^{KO} HFD $n = 12$), (**I**) infrared thermal images and quantification of BAT interscapular temperature (WT CD and MCJ^{KO} CD $n = 10$; WT HFD and MCJ^{KO} HFD $n = 6$). **J** Representative histology of BAT lipid content and quantification of lipid droplet average area (WT CD and MCJ^{KO} CD $n = 5$; WT HFD and MCJ^{KO} HFD $n = 5$). Scale bar: 100 µm. Statistical differences according to a two-sided Student´s *t* test (**A**, **B**, **E**), one-way ANOVA followed by Tukey's multiple comparison test (**D**, **F**, **G**, **I**, **J**) or two-way ANOVA followed by Sidak's multiple comparison test (**E**, **H**), and analysis of two-way covariance (ANCOVA) with body weight as covariate (**H**). Values are represented as the mean ± SEM. Source data are provided as a Source Data file. AUC area under curve, BAT brown adipose tissue, CD chow diet, EE energy expenditure, HFD high fat diet, WATsc subcutaneous white adipose tissue.

https://doi.org/10.1038/s41467-024-54353-4

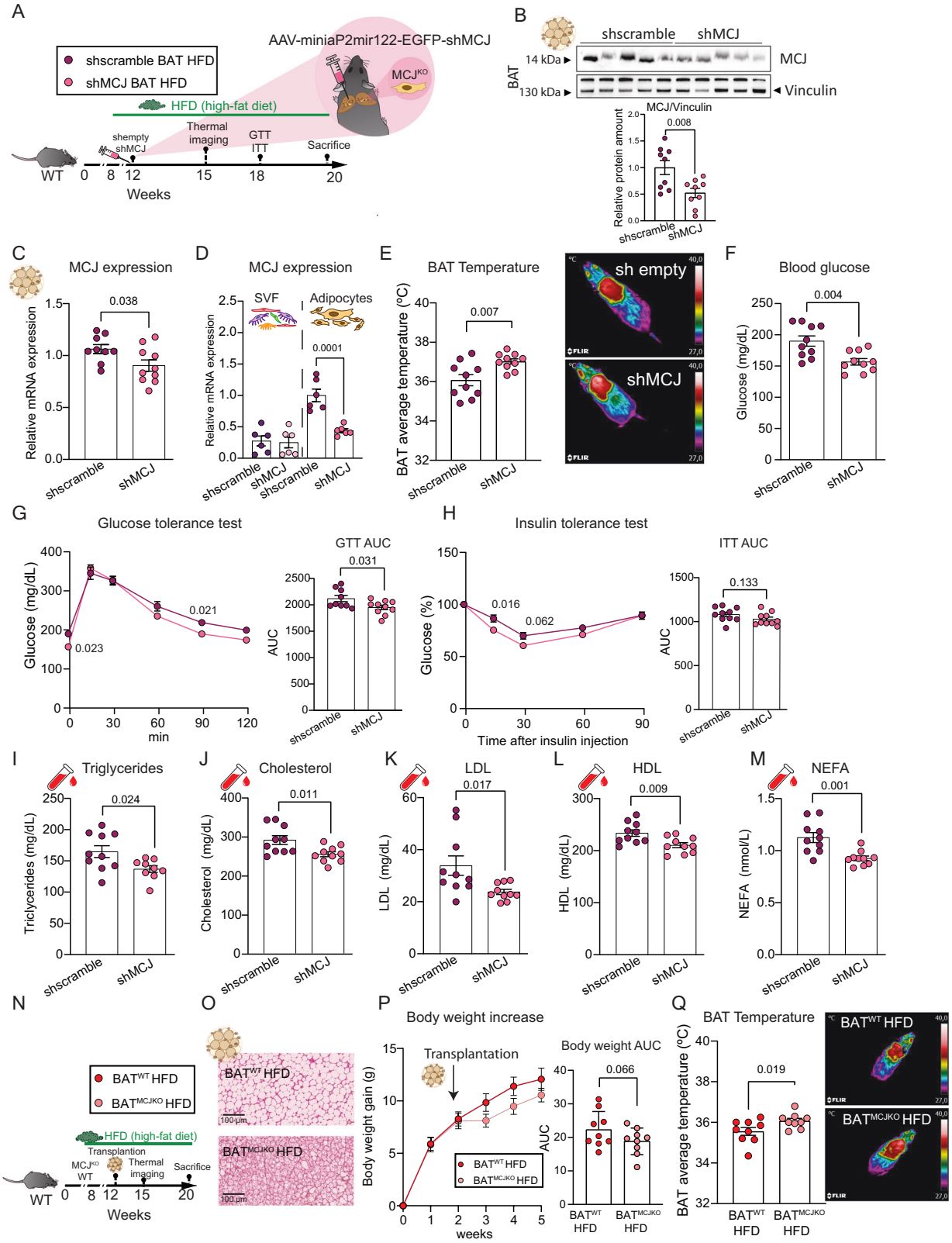

reported[28], with reduced lipid droplets content in mice transplanted with MCJ^{KO} BAT (referred to as BAT^{MCJKO}) compared to the one coming from WT mice BAT^{WT} (Fig. 2O). Furthermore, BAT transplantation with MCJ^{KO} BAT led to a decrease in body weight gain and an increase in interscapular temperature (Fig. 2P, Q). Collectively, these results affirm that BAT-specific MCJ deficiency enhances BAT temperature and protects against diet-induced obesity. This emphasizes the potential of MCJ as a therapeutic target for combating obesity.

Increased BAT fatty acid oxidation and glycolysis in MCJ-deficient mice

Our data strongly suggest that MCJ plays a significant role in BAT metabolism. Further examination of BAT and WATsc metabolism

Fig. 2 | BAT-specific MCJ deficiency increases BAT temperature protecting against obesity. A pAAV-miniaP2mir122-EGFP-shMCJ or control pAAV-miniaP2mir122-EGFP-shscramble HFD-fed mice for 12 weeks injected at the 3rd week of HFD. **B** Representative immunoblot analysis showing MCJ deletion in BAT lysate (shscramble and sh MCJ $n = 9$). Vinculin protein expression was monitored as a loading control. qRT-PCR analysis of MCJ mRNA expression in BAT (**C**) (shscramble $n = 9$; sh MCJ $n = 10$) and in the stromal vascular or adipocyte fraction (**D**) (shscramble and sh MCJ $n = 6$). mRNA expression was normalized to the amount of *Gapdh* mRNA. **E** Infrared thermal images and quantification of BAT interscapular temperature (shscramble and sh MCJ $n = 10$). **F** Blood glucose levels (shscramble and sh MCJ $n = 10$). **G** Glucose tolerance test (GTT) and area under the curve (AUC) (shscramble $n = 9$; sh MCJ $n = 10$). **H** Insulin tolerance test (ITT) expressed as a percentage of the baseline value and AUC (shscramble and sh MCJ $n = 10$). **I**–**M** Concentrations of triglycerides, total cholesterol, LDL, HDL and NEFA were determined in submandibular blood samples (shscramble $n = 10$; sh MCJ $n = 10$ except in Fig1I $n = 9$). **N** After 3 weeks of exposure to HFD, WT mice were transplanted with BAT from MCJ^{KO} or WT mice. **O** Representative histology of BAT lipid content (BAT^{WT} and BAT^{MCJKO} $n = 9$). Scale bar: 100 µm; (**P**) body weight time course and area under the curve over 5 weeks (BAT^{WT} and BAT^{MCJKO} $n = 9$); (**Q**) infrared thermal images and quantification of BAT interscapular temperature (BAT^{WT} and BAT^{MCJKO} $n = 9$). Statistical differences according to a two-sided Student´s *t* test (**B**, **C**, **E**, **F**, **G**, **H**, **I**, **J**, **K**, **L**, **M**, **P**, **Q**), one-way ANOVA followed by Tukey's multiple comparison test (**D**) and two-way ANOVA followed by Sidak's multiple comparison test (**G**, **H**, **P**). Values are represented as the mean ± SEM. Source data are provided as a Source Data file. AUC area under curve, BAT brown adipose tissue, GTT glucose tolerance test, HDL high density lipoprotein, HFD high fat diet, ITT insulin tolerance test, LDL low density lipoprotein, NEFA non-esterified fatty acids, SVF stromal vascular fraction.

through the measurement of ^{14}C-palmitate oxidation revealed an increase in fatty acid oxidation (FAO) in MCJ^{KO} BAT and WATsc. This was evidenced by elevated levels of CO_2, resulting from complete oxidation through the tricarboxylic acid cycle (TCA cycle) (Fig. 3A and Supplementary Fig. 3A). Additionally, the expression levels of multiple enzymes involved in FAO were significantly elevated in HFD-fed MCJ^{KO} BAT while no differences were found in WATsc (Fig. 3B and Supplementary Fig. 3B, C).

There was also an increase in glycolytic flux in MCJ^{KO} BAT, indicated by the lactate production and the conversion of [3-^{3}H] glucose into ^3H_2O during triose-phosphate isomerase production (Fig. 3C). However, these parameters were decreased in MCJ^{KO} WATsc (Supplementary Fig. 3D). In fact, we could demonstrate that there was more glucose uptake by the brown adipocytes MCJ^{KO} measured in the BAT1 cell line (Supplementary Fig. 3E, F). This phenomenon aligns with a unique metabolic characteristic of BAT: while in other tissues FAO and glycolysis often inhibit each other, as did in the WATsc, both processes can remain active simultaneously during BAT activation, effectively mitigating ATP depletion[29].

Increased interscapular temperature by an UCP1-independent mechanism

Moreover, the activation of BAT in MCJ^{KO} mice was further confirmed by the increased expression of genes associated with thermogenesis (Fig. 3D), including the β3 adrenergic receptor (Adrβ3). The relevance of this pathway in enhancing thermogenesis in MCJ^{KO} BAT was confirmed through the administration of the Adrβ3 antagonist SR59230A (Fig. 3E). Following Adrβ3 inhibition, no differences in interscapular temperature were observed between MCJ^{KO}-treated mice and WT mice (Fig. 3F). Although it is known that the activation of Adrβ3 can lead to an increase in UCP1 expression[30], both UCP1 mRNA and protein levels remained unchanged between genotypes in BAT and WATsc (Fig. 3D, G and Supplementary Fig. 4A, B), as did lipolytic genes in WATsc (Supplementary Fig. 4B). We found neither alteration in alternative thermogenic pathways such as creatine kinase (CK), the sarco/endoplasmic reticulum calcium ATPase (SERCA), and the lipid futile cycle (Supplementary Fig. 4C, D)[13,14].

To determine whether BAT activation was independent of UCP1, we crossed MCJ^{KO} mice with $UCP1^{KO}$ mice. We confirmed that there were no phenotypic differences under CD, presenting the same body weight, body composition and BAT temperature between $UCP1MCJ^{KO}$ and the rest of the genotypes (Supplementary Fig. 4E–I).

However, $UCP1MCJ^{KO}$ mice showed decreased body weight and fat mass, without changes in lean mass, after HFD compared to $UCP1^{KO}$ mice (Fig. 3H–K), as well as a higher interscapular temperature (Fig. 3L). The comparison of $UCP1MCJ^{KO}$ with MCJ^{KO} indicates that they present the same body weight and fat mass, suggesting that loss of UCP1 did not affect the protection against obesity. Additionally, we found that $UCP1^{KO}$ mice displayed lower BAT temperature, which was reverted in $UCP1MCJ^{KO}$ mice after HFD. Collectively, these data suggest that MCJ might control thermogenesis at least in part through a UCP1-independent mechanism.

Mitochondria from MCJ^{KO} resembles BAT activation

To gain deeper understanding of the molecular mechanism by which MCJ controls BAT thermogenesis, we conducted an electron microscopy analysis to examine mitochondrial morphology. Intriguingly, we observed a higher number of mitochondria with a distinctive rounder shape in MCJ^{KO} BAT (Fig. 4A). This morphology is typically associated with BAT activation, facilitating the uptake of free fatty acids (FFA)[31], as we corroborated by analyzing the morphology of acute cold-exposed mitochondria (Fig. 4A). Our findings were further supported by proteomic analysis, which revealed an increase in proteins involved in mitochondrial fission and a decrease of fusion proteins, coherent with the observed alterations in mitochondrial shape during cold exposure (Supplementary Fig. 5A). Noticeably, parameters such as mitochondrial area, and cristae density (Supplementary Fig. 5B, C) remained unchanged. The transition to a rounder form could indicate a shift toward increased fatty acid oxidation[31], a process that provides a stable energy source. Thereby, in a context of persistent nutrient overload which may lead to cold intolerance and metabolic inflexibility, this transition might help to minimize electron leakage[32] and indirectly contribute to reduced ROS production, as observed in (Supplementary Fig. 5D). Despite the changes in mitochondrial morphology, the mtDNA/nDNA ratio and the levels of OXPHOS proteins, as quantified by western blotting, remained unchanged, indicating that the overall quantity of mtDNA and mitochondrial protein was stable (Supplementary Fig. 5E, F). Additionally, we observed no changes in the components of mitophagy signaling (Supplementary Fig. 5G).

In terms of mitochondria functionality, our observations indicate that brown fat SVFs derived from MCJ^{KO} mice exhibit higher basal respiration, ATP-linked respiration and maximum respiration (Fig. 4B). We also analyzed the lipid content and, just as observed in the phenotype of MCJ^{KO} mice, we observed a decreased oil red staining (Fig. 4C). Therefore, we conducted a fatty acid oxidation seahorse test with palmitate as substrate using plate based respirometry where we observed higher basal respiration, ATP-linked respiration and maximum respiration (Fig. 4D). These findings suggest that MCJ deletion may result in enhanced mitochondrial respiration, reducing fat accumulation.

Our results suggest that BAT mitochondria from MCJ^{KO} mice show typical characteristics of activated BAT. To determine whether these morphological changes translate to molecular changes in the mitochondria we performed unbiased proteomic analysis of isolated BAT mitochondria from MCJ^{KO} and WT mice comparing them with isolated BAT mitochondria after acute cold exposure. Consistent with the higher FAO observed in BAT from MCJ^{KO} mice (Fig. 3A), we detected elevated levels of enzymes involved in FAO in the MCJ^{KO} BAT mitochondria. Additionally, proteomic analysis indicated an activation of the branched chain amino acid (BCAA) degradation enzymes to fuel

https://doi.org/10.1038/s41467-024-54353-4

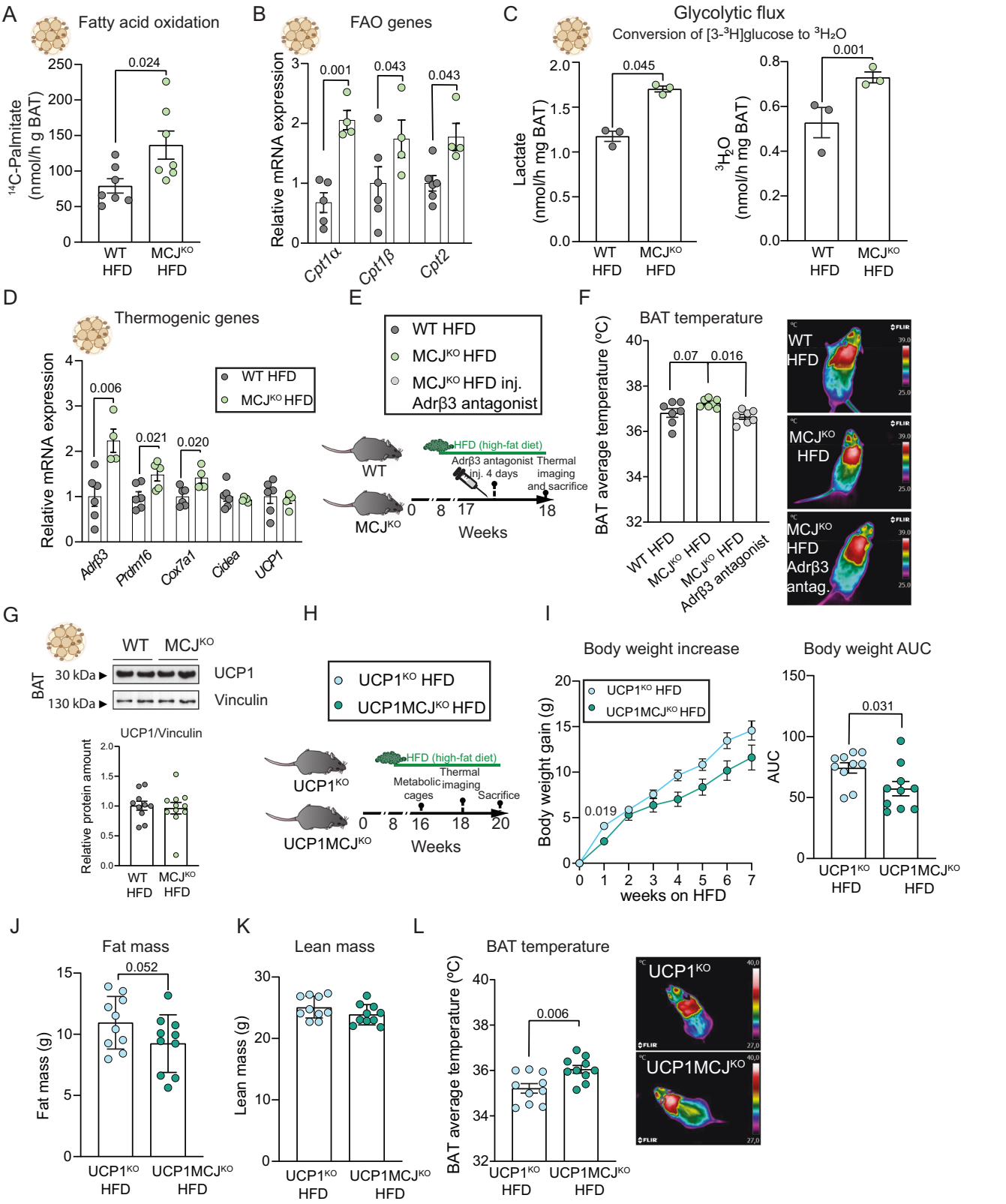

the TCA cycle (Supplementary Fig. 5H). To further evaluate whether these changes also occur in human activated BAT, we compared our results with databases of cold-exposed human BAT[33]. Our findings confirmed an increase in proteins involved in FAO, BCAA and TCA (Supplementary Fig. 5I), resembling the metabolic changes that appear in human mitochondria from activated BAT[33].

It has been shown that activated BAT mitochondria from mice and humans actively utilize BCAAs for thermogenesis and promote BCAA clearance[34]. Given the observed alteration in mitochondrial amino acid degradation pathways, we explored the metabolomic landscape, revealing that amino acid metabolites of MCJ^{KO} are highly decreased (Supplementary Fig. 6).

Fig. 3 | Increased BAT FAO and glycolysis in MCJ-deficient mice, UCP1-independent thermogenesis. A–D HFD-fed WT and MCJ^{KO} male mice (8 wk-old) were sacrificed. **A** Fatty acid β-oxidation was determined by the conversion of [^{14}C]-palmitate to [^{14}C]-CO_2 in BAT (WT and MCJ^{KO} $n = 7$); (**B**) qRT-PCR analysis of mRNA expression of fatty acid oxidation carriers from BAT. mRNA expression was normalized to the amount of *Gapdh* mRNA (WT $n = 6$ except in cpt1α $n = 5$; MCJ^{KO} $n = 4$); (**C**) Glycolysis was measured by the lactate production and the conversion of [3-^{3}H]-glucose to [^3H_2O] in BAT (WT and MCJ^{KO} $n = 3$); (**D**) qRT-PCR analysis of browning genes mRNA expression from BAT isolated (WT $n = 6$; MCJ^{KO} $n = 5$ except in Adrβ3 and Cox7a1 $n = 4$). mRNA expression was normalized to the amount of *Gapdh* mRNA; (**E**) WT and MCJ^{KO} male (8 wk-old) mice were HFD-fed for 10 weeks and injected with Adrβ3 antagonist SR59230A 3 mg/kg/day for 4 days. **F** Infrared thermal images and quantification of BAT interscapular temperature (WT and MCJ^{KO} $n = 7$). **G** Representative immunoblot analysis showing UPC1 expression in BAT lysate from HFD-fed WT or MCJ^{KO} mice (WT $n = 10$; MCJ^{KO} $n = 11$). Vinculin protein expression was monitored as a loading control. **H** UCP1^{KO} and UCP1MCJ^{KO} male mice (8 wk-old) were HFD-fed for 12 weeks. **I** Body weight time course and area under the curve over 8 weeks (UCP1^{KO} and UCP1MCJ^{KO} $n = 10$), (**J**) fat mass (UCP1^{KO} and UCP1MCJ^{KO} $n = 10$), (**K**) lean mass (UCP1^{KO} and UCP1MCJ^{KO} $n = 10$) and (**L**) infrared thermal images and quantification of BAT interscapular temperature (UCP1^{KO} and UCP1MCJ^{KO} $n = 10$). Statistical differences according to a two-sided Student´s *t* test (**A**, **C**, **D**, **G**, **I**, **J**, **K**, **L**), one-way ANOVA followed by Tukey's multiple comparison test (**F**) and two-way ANOVA followed by Sidak's multiple comparison test (**B**, **I**). Values are represented as the mean ± SEM. Source data are provided as a Source Data file. Adrβ3 beta-3 adrenergic receptor, BAT brown adipose tissue, Cidea cell death inducing DFFA like effector A, Cox7a1 cytochrome C oxidase subunit 7A1, Cpt carnitine palmitoyltransferase, FAO fatty acid oxidation, HFD high fat diet, Prdm16 PR domain containing 16, UCP1 uncoupling protein 1.

eIF2α mediates elevated thermogenesis in MCJ^{KO} mice

Amino acids deprivation is known to induce a stress response that has been linked to activation of thermogenesis[35,36]. Indeed, our mitochondrial proteomic analysis showed elevated mitochondrial stress, including an upregulation of eIF2α signaling, resembling the response to acute cold exposure (Fig. 4E and Supplementary Fig. 7A). Western blotting of BAT homogenates confirmed that the levels of active, phosphorylated eIF2α, were elevated in MCJ^{KO} BAT as observed in WT BAT under acute cold conditions (Fig. 4F).

To elucidate the role of eIF2α in the metabolic phenotype, we specifically deleted eIF2α in BAT using CRISPR technology (Fig. 4G). Its deletion in MCJ^{KO} BAT effectively reversed the protection against diet-induced body weight gain (Fig. 4H). Moreover, it counteracted the increased interscapular temperature observed in MCJ^{KO} mice (Fig. 4I) and the decreased lipid droplets accumulation (Fig. 4J), providing strong evidence that eIF2α was responsible for the increased thermogenesis. To further study the mechanisms responsible for the increased thermogenesis, we compared the proteomes from HFD-fed eIF2α^{KO} and eIF2α/MCJ^{KO} mice with MCJ^{KO} and WT mice. The main pathways, which we previously found to be upregulated in the mitochondria of BAT in our MCJ^{KO} mice, such as FAO, TCA, BCCA and mitochondrial stress response, were downregulated in both eIF2α^{KO} and eIF2α /MCJ^{KO} mice (Supplementary Fig. 7B, C). This suggests that eIF2α plays a key role in activating these pathways. These findings underscore the critical role of eIF2α signaling in mediating the thermogenic effects of MCJ deficiency in BAT.

In conclusion, our study unveils the pivotal role of MCJ in regulating BAT thermogenesis and metabolism. We demonstrate that MCJ deficiency promotes a marked increase in BAT thermogenesis, protecting against diet-induced obesity by enhancing energy expenditure. Mechanistically, the absence of MCJ triggers mitochondrial remodeling and stress, culminating in the activation of eIF2α signaling, which, in turn, drives the thermogenic response (Supplementary Fig. 7D).

Discussion

BAT has emerged as a promising target in the battle against obesity, offering emerging avenues for the activation of non-shivering thermogenesis. Understanding the molecular mechanisms governing BAT function holds therapeutic potential. Here we found that mice lacking mitochondrial protein MCJ specifically in the BAT exhibited a significant increase in thermogenesis. We used a miniaturized version of the aP2 promoter (mini/aP2) fused with miR122 to avoid expression in other cell types other than adipocytes[25]. The increased thermogenesis was characterized by heightened glycolysis and FAO within the BAT. These findings are particularly intriguing since they occurred without any notable changes in the expression of UCP1, a protein classically linked to the functionality of BAT thermogenesis[12]. This implies that the elevated thermogenesis in these mice operates independently of UCP1, challenging the traditional notions of BAT thermogenic processes. This independence was further substantiated when mice lacking both UCP1 and MCJ displayed elevated thermogenesis, indicating that the increase in BAT thermogenesis was mediated by alternative thermogenic mechanisms. In recent years, alternative pathways of thermogenesis have been identified, including futile cycles like the CK and the SERCA cycle, which have been shown to generate heat without relying on UCP1[37]. Moreover, recent research has shown that brown adipocytes can activate increased energy expenditure through enhanced lipid cycling[38].

While we did not observe differences in the already described independent UCP1 pathways, our findings indicate that the absence of MCJ enhances the catabolism of amino acids, proposing a different mechanism for inducing thermogenesis. These findings open an exciting promising frontier in our understanding of BAT's role in controlling energy expenditure and offer promising avenues for exploring non-UCP1-dependent thermogenic processes.

Our results in humans and mice suggest that the reduction of MCJ observed in patients with obesity appears to act as a compensatory mechanism to enhance BAT thermogenesis. This adaptation may serve as a protective strategy to counteract excessive weight gain. Notably, this is not an isolated instance; p38α, a substantial regulator of thermogenesis, exhibits an inverse correlation with BMI and, when deleted, promotes thermogenesis[9]. There is much more to uncover and comprehend about the compensatory responses that emerge during obesity in BAT. Gaining knowledge about these mechanisms holds the key to novel approaches for combatting obesity and metabolic disorders.

Mechanistically, mice deficient in MCJ displayed clear signs of stress responses in mitochondria, marked by an upregulation amino acids degradation and activation of proteasomal eIF2α-dependent proteins within mitochondrial BAT. Indeed, the upregulation of FAO and BCCA pathways are controlled by eIF2α implying that the activation of eIF2α in MCJ^{KO} mice controls the decrease in body weight and the activation of thermogenesis. It has been demonstrated that upon activation, BAT relies on BCAA for thermogenesis leading to a clearance in mice and humans[33,34], protecting for diet-induced obesity. This observation aligns with previous research that has emphasized the pivotal role of proteasomal activation for enhancing thermogenesis[39]. It has been described that BAT exhibits increased proteasomal activity under specific conditions, such as exposure to cold temperatures (4 °C) or moderate room temperatures (22 °C)[40]. In fact, cold adaptation triggers the activation of nuclear factor erythroid derived 2-related factor 1 (Nrf1), a transcription factor necessary for induced proteasome in BAT. This activation boosts proteasomal activity, which is vital for maintaining ER stability and cellular integrity during high thermogenic activity. In fact, deleting Nrf1 in mice led to whitening of BAT, emerging as a guardian of brown adipocyte function for adapting to cold or to obesity. However, neither conditional deletion of adipocyte inositol-requiring enzyme 1 (IRE1) nor X-box binding protein 1 (XBP1) impact non-shivering thermogenesis in mice[40]. Moreover,

https://doi.org/10.1038/s41467-024-54353-4

deficiency of leucine rich pentatricopeptide repeat containing (Lrpprc) in BAT activates transcription factor 4 (ATF4) and promotes proteome turnover in BAT, improving cold tolerance in normal and Ucp1 knockout mice. This mechanism reveals a diet-dependent, Ucp1-independent thermogenic mechanism[36].

However, while hyperphosphorylation of eIF2α has been associated with impaired thermogenesis in BAT in Ssu72 deficient mice[41], it has not been conclusively demonstrated that these defects are eIF2α-mediated. It is plausible that other functions of this vital phosphatase in RNA processing, transcription, and mRNA capping may play a mediating role in this effect.

These findings shed promising light on the regulatory mechanisms underlying BAT function and provide insights into potential therapeutic targets for combating obesity and related metabolic

Fig. 4 | The absence of MCJ alters mitochondria to increase thermogenesis by resembling cold-exposed BAT with increased mitochondrial stress response. **A** HFD-fed WT and MCJ^{KO} male mice (8 wk-old) were sacrificed at RT or after acute cold exposure. Electron microscopy quantifying mitochondrial roundness (WT $n = 12$; MCJ^{KO} $n = 10$; WT 4 °C $n = 8$ images) and number (WT, MCJ^{KO} and WT 4 °C $n = 9$ images) per 3 mice. Scale bar: 2 µm; (**B**–**D**) respiratory analysis was performed in differentiated brown adipocytes isolated from BAT of WT or MCJ^{KO} mice: (**B**) oxygen consumption rate (WT $n = 6$; MCJ^{KO} $n = 5$ wells). Nonmitochondrial respiration was subtracted, all values were normalised to protein content. **C** Absorbance of dissolved oil red staining (WT and MCJ^{KO} $n = 15$ wells). **D** OCR stimulated with palmitate or BSA (WT and MCJ^{KO} $n = 4$ wells). Nonmitochondrial respiration was subtracted, all values were normalised to protein content. **E**, **F** HFD-fed WT and MCJ^{KO} male mice (8 wk-old) were sacrificed at RT or after acute cold exposure. **E** Heatmap of BAT mitochondria proteomic expression as z score for the normalized CPM representing mitochondrial stress pathways (WT $n = 5$; MCJ^{KO} $n = 4$); (**F**) representative BAT lysate immunoblot of the phosphorylation of eIF2α (WT and MCJ^{KO} $n = 12$; WT 4 °C $n = 9$). Tubulin protein expression was monitored as loading control. **G** WT, MCJ^{KO}, eIF2α^{KO} and eIF2αMCJ^{KO} male (8 wk-old) mice were HFD-fed for 12 weeks. **H** Body weight time course and area under the curve (WT and eIF2αMCJ^{KO} $n = 7$; eIF2α^{KO} and MCJ^{KO} $n = 8$); (**I**) infrared thermal images and quantification of BAT interscapular temperature (WT and MCJ^{KO} $n = 7$; eIF2α^{KO} and eIF2αMCJ^{KO} $n = 8$); (**J**) representative histology of BAT lipid content (WT, MCJ^{KO}, eIF2α^{KO} and eIF2αMCJ^{KO} $n = 7$). Scale bar: 100 µm. Statistical differences according to a two-sided Student´s t test (**C**), one-way ANOVA followed by Tukey's multiple comparison test (**A**, **F**, **H**, **I**, **J**) and two-way ANOVA followed by Sidak's multiple comparison test (**B**, **D** comparing palmitate incubated groups, **H**). Values are represented as the mean ± SEM. Source data are provided as a Source Data file. AUC area under curve, eIF2α eukaryotic initiation factor2A, FCCP carbonyl-cyanide p-(trifluoromethoxy)phenylhydroazone, HFD high fat diet, OCR oxygen consumption rate, RT room temperature.

disorders. Overall, our work underscores MCJ as a promising candidate for the development of interventions aimed at harnessing the substantial thermogenic potential of BAT to combat obesity and its associated complications.

Methods

Ethics statement

This population study was approved by the Ethics Committee of the University Hospital of Salamanca and the Carlos III (CEI PI 09_2017-v3) with all subjects providing written informed consent to undergo subcutaneous fat biopsy under direct vision during surgery. Data were collected on demographic information (age, sex, and ethnicity), anthropomorphic measurements (BMI), smoking and alcohol history, coexisting medical conditions, and medication use. All animal procedures conformed to EU Directive 86/609/EEC and Recommendation 2007/526/EC regarding the protection of animals used for experimental and other scientific purposes, enacted under Spanish law Real Decreto 53/2013. The protocols are CNIC-07/18 and PROEX 215/18.

Mice

MCJ^{KO} and UCP1^{KO} (B6.129-Ucp1tm1Kz/J)[19,42] male mice were backcrossed for 10 generations to the C57BL/6 J background (Jackson Laboratory). Polymerase chain reaction (PCR) analysis of genomic DNA confirmed the genotypes. Mice were cohoused under a 12 h light/12 h dark cycle in a specific pathogen-free facility. In all experiments, male mice between 8 and 20 weeks old were used. Mice were fed a chow diet (CD) (Altromin, no. 1410) or a high-fat diet (HFD) (Research Diets, no. D11103002i) for 8–10 weeks. Body weight was measured weekly during the experimental phase in all experiments. Pharmacological inactivation of Adrβ3-receptor was performed by subcutaneous injection of the SR59230A (Tocris) antagonist 3 mg/kg/day for 4 days. For thermoneutral experiments, 8-week-old mice were kept at 30 °C for 8 weeks. For acute cold exposure experiments, 8-week-old mice were kept at room temperature for 8 weeks and then transferred to a cold incubator at 4 °C for 4 h.

To choose the size of the sample, we have used the 3 R rule to ensure statistical validity and significance with the chosen size. Centro Nacional de Investigaciones Cardiovasculares (CNIC) has biostatisticians who use statistical methods to ensure that the correct number of animals will be employed in each experiment to detect significant biologically relevant differences. We used 3–11 mice per group for at least 80% power for one- and two-sided testing. Animals that presented disease or had been bitten because of a fight in the cage were excluded. The exact number of animals used in each experiment is detailed in the corresponding figure legend.

Human samples

The study population included 135 patients (114 adult patients with BMI ≥ 35) who underwent elective bariatric surgery at the University Hospital of Salamanca. Control subjects (21 adults with BMI ≤ 30) were patients who underwent laparoscopic cholecystectomy for gallstone disease. Before surgery, fasting venous blood samples were collected for measuring complete cell blood count, aspartate aminotransferase (AST), alanine aminotransferase (ALT), total cholesterol, high-density lipoprotein, low-density lipoprotein, triglycerides, alkaline phosphatase, glucose, and albumin (Table 1).

Indirect calorimetry system

Energy expenditure, respiratory exchange, locomotor activity, and food intake were quantified using the indirect calorimetry system (PanLab v3.0 and TSE LabMaster, TSE Systems) over 2 days[43].

BAT temperature

BAT-adjacent interscapular temperature was quantified by thermographic imaging using a FLIR T430sc Infrared Camera (FLIR Systems, Inc., Wilsonville, Oregon) and analyzed with FLIR software[44].

Magnetic resonance imaging and nuclear magnetic resonance spectroscopy

Body fat and lean mass were quantified by nuclear magnetic resonance imaging using a Whole-Body Composition Analyzer (EchoMRI, Houston, Texas)[45].

Table 1 | Characteristics of patients and controls for human subcutaneous fat samples

Variable	Patients with obesity ($n = 114$)	Controls ($n = 21$)	P value
Age (years)	47.69 (10.59)	49.33 (17.08)	0.584
Female:male ratio	82:32	13:8	0.298
BMI (kg/m^2)	47.36 (7,01)	24.34 (2.43)	<0.0001
Fasting blood sugar (mg/dL)	116.02 (45.66)	90.45 (12.84)	0.014
AST (IU/L)	21.92 (11.29)	27.00 (27.05)	0.213
ALT (IU/L)	29.40 (20.92)	73.50 (169.39)	0.022
Alkaline phosphatase	71.96 (20.69)	87.67 (30.32)	0.014
Albumin (mg/dL)	4.33 (0.30)	4.49 (0.46)	0.058
Total cholesterol (mg/dL)	182.14 (35.60)	190.67 (50.15)	0.438
Triglycerides (mg/dL)	142.01 (74.99)	119.25 (52.33)	0.268
LDL-cholesterol (mg/dL)	105.75 (31.87)	121.69 (41.43)	0.119
HDL-cholesterol (mg/dL)	48.57 (15.77)	49.74 (16.11)	0.808

Variables are presented as mean (standard deviation) are compared by means of two-sided Student t test.
BMI body mass index, *AST* aspartate aminotransferase, *ALT* alanine aminotransferase.

Adenoviral vector production and administration

The adeno-associated virus (AAV either pAAV-miniaP2mir122-EGFP-shMCJ or pAAV-miniaP2mir122-EGFP-shscramble) was packaged into AAV-9 capsids with the use of pAdDF6 helper plasmids transfected into HEK293A cells by calcium-phosphate coprecipitation. A total of 840 µg plasmid DNA (mixed in an equimolar ratio) were used per HYPERFlask (Corning) seeded with 1.2×10^8 cells the day before. Seventy-two hours after transfection, the cells were collected by centrifugation and the cell pellet was resuspended in 50 mM Tris HCl, 150 mM NaCl, 2 mM $MgCl_2$ buffer on ice before digestion with DNase I and RNaseA (0.1 mg/mL: 1 each; Roche) at 37 °C for 60 min. Clarified supernatant containing the viral particles was obtained by iodixanol gradient centrifugation. Gradient fractions containing virus were concentrated using Amicon UltraCel columns (MilliporeSigma) and stored at −70 °C[46]. Recombinant AAV9 were tittered and 1×10^9 virus particles per mouse in PBS expressing were injected in a volume of 50 µl bilaterally into the BAT in mice under sevoflurane anesthetics[47].

Lentivirus production and administration

Transient calcium phosphate co-transfection of HEK-293T cells was carried out with pLV[CRISPR]-hCas9:T2A:Puro-U6>meif2a[gRNA#1849] and pLV[CRISPR]-hCas9:T2A:Puro-U6>meif2a[gRNA#1159] from Vector Builder, together with pΔ8.9 and pVSV-G packaging plasmids. Supernatants containing the lentiviral particles were collected 48 h and 72 h after removal of the calcium phosphate precipitate, centrifuged at 700 × *g* at 4 °C for 10 min, and concentrated (×165) by ultracentrifugation for 2 h at 121,986 × *g* at 4 °C (Ultraclear Tubes, SW28 rotor and Optima L-100 XP Ultracentrifuge; Beckman)[48]. Viruses were resuspended in cold sterile PBS and titrated by qRT-PCR. Lentivirus were tittered and 1×10^9 virus particles per mouse in PBS expressing were injected in a volume of 50 µl bilaterally into the BAT in mice under sevoflurane anesthetics[47].

BAT transplantation

BAT was removed from the interscapular region of anesthetized WT or MCJ^{KO} donor mice, washed with sterile PBS and divided into 4 small pieces to ensure vascularization of the implanted tissue. Then, BAT was implanted subcutaneously in the interscapular region of recipient WT after removal of their own interscapular BAT[49].

Glucose tolerance tests (GTT) and insulin tolerance tests (ITT)

For GTT, mice were fasted overnight (16 h), whereas for the ITT mice were fed ad libitum, and basal glucose concentration was measured in tail-tip blood with a glucometer (Ascensia BREEZE 2 or Ascensia Contour Next One). Mice were then injected intraperitoneally (i.p.) with D (+)-glucose monohydrate (Merck) dissolved in saline buffer for the GTT, and with insulin (0.75 U/kg body weight) (Lilly) for the ITT. Blood glucose concentration was measured at 15, 30, 60, 90, and 120 min post injection[50].

Biochemistry parameters

Submandibular blood samples were collected in EDTA blood collection tubes (Microvette) and centrifuged (10,000 × *g* for 20 min at 4 °C) for serum separation. Concentrations of triglycerides, total cholesterol, LDL, HDL and NEFA were determined by using an automated analyzer according to the manufacturers' instructions.

Histology

BAT samples were fixed in 10% formalin for 48 h, dehydrated, and embedded in paraffin. Sections (5 µm) were cut and stained with hematoxylin and eosin (Sigma-Aldrich, no. H3136 and Thermo Fisher Scientific, no. 6766008). Sections were examined with a Leica DM2500 microscope fitted with a 20X objective. Images were quantified by Cellpose coupled to ImageJ software. Fat droplets were detected by oil red staining (0.7% in propylenglycol) in differentiated brown adipocytes. Oil red was dissolved in isopropanol and measured at 518 nm.

Fatty acid oxidation

Pieces of BAT and WATsc (30 mg) were homogenized in a Potter homogenizer (5 strokes) in cold buffer (25 mM Tris–HCl, 500 nM sucrose, 1 mM EDTA-Na_2 (pH 7.4)) and sonicated for 10 s. Homogenates were centrifuged at 420 × *g* for 10 min at 4 °C. Samples (60 µl) from the homogenate supernatant were used for the assay, which started by adding 340 µl of assay mixture (500 µM palmitate/0.4 µCi [1–14 C] palmitate per reaction). Samples were incubated for 30 min at 37 °C with shaking in tubes with a Whatman filter-paper circle in the cap. The reaction was stopped by adding 200 µl of 1 M perchloric acid, and 45 µl of 1 M sodium hydroxide was added to impregnate the Whatman cap. After 1 h at room temperature, the Whatman caps (containing released CO_2) were removed, and the radioactivity associated was measured in a scintillation counter. Tubes were centrifuged at 21,000 × *g* for 10 min at 4 °C, and samples (400 µl) were collected from the supernatant (containing ASMs). Radioactivity was counted in a scintillation counter[51,52].

Determination of glycolytic flux

The glycolytic flux was estimated by determining the rate of conversion of D-[3-^{3}H]glucose into ^3H_2O, which, previously validated[53,54], assesses the rate of ^{3}H of C^3-glucose interchange with water at triose-phosphate isomerase. BAT or WATsc slices (10–40 mg) were pre-incubated for 30 min in 2 ml of a Krebs–Henseleit buffer (11 mM Na_2HPO_4, 122 mM NaCl, 3.1 mM KCl, 0.4 mM KH_2PO_4, 1.2 mM $MgSO_4$, 1.3 mM $CaCl_2$; pH (7.4) supplemented with 5.5 mM D-glucose at 37 °C, followed by incubation in the presence of 5 µCi/ml of D-[3-^{3}H]glucose in fresh Krebs–Henseleit buffer (2 ml) in glass 25-ml Erlenmeyer flasks equipped with a central well containing a tube with 0.5 ml of water. The flask atmosphere was gassed with a O_2/CO_2 (95/5) mixture for 20 s and stopped with a rubber cap, and the flasks were incubated in a thermostatized orbital shaker (Forma Benchtop Orbital Shaker, Model 420, Thermo Fisher) for 3 h at 37 °C. ^3H_2O collected in the tube placed in the central well was linear with time up to at least 4 h. Incubations were finished by injecting 0.2 ml of 20% (v/v) $HClO_4$ through the rubber cap, and flasks were further incubated for 72 h to allow the equilibration of ^3H_2O between the incubation medium and the water of the central well. The rate of glycolysis was expressed as nmol of D-[3-^{3}H] glucose converted into ^3H_2O per hour and per mg tissue[55].

Determination of lactate concentration

Lactate concentrations were measured in the same buffer as the glycolytic flux after the 3 h incubation period spectrophotometrically by determining the increments in absorbance at 340 nm in a mixture containing 1 mM NAD^+ and 22.5 U/ml lactate dehydrogenase in 0.25 M glycine/0.5 M hydrazine/1 mM EDTA buffer at pH 9.5.

Western blot

Samples were lysed using Triton lysis buffer [20 mM Tris (pH 7.4), 1% Triton X-100, 10% glycerol, 137 mM NaCl, 2 mM EDTA, 25 mM β-glycerophosphate, 1 mM sodium orthovanadate, 1 mM phenylmethylsulphonyl fluoride, and 10 µg/mL aprotinin and leupeptin]. Extracts (20–50 µg protein) were examined by immunoblot. Primary (1:1000) and secondary antibody (1:5000) used in the study are listed in reporting summary. Reactive bands were detected by chemiluminescence and analysed using Image-J software (National Institutes of Health).

qRT-PCR

RNA was extracted with the RNeasy Plus Mini kit or RNeasy Plus Micro kit (Quiagen, no. 74106 or no. 217084) and transcribed to

complementary DNA (Applied Biosystems, no. 4368814). Real Time qRT-PCR was performed using Fast SYBR Green probe (Applied Biosystems, no. 4385616) and appropriate primers in a 7900 Fast Real Time thermocycler (Applied Biosystems). Primers and Taqman probe are listed below:

h_GAPDH Fw CCATGAGAAGTATGACAACAG
h_GAPDH Rv GGGTGCTAAGCAGTTGGTG
h_MCJ Fw TTGCAGGTCGCTACGCATTT
h_MCJ Rv CCAGCTTCTCGCCTACTCAT
m_Adrb3 Fw TGAAACAGCAGACAGGGAC
m_Adrb3 Rv TCTTGACACTCCCTCAGCAC
m_Cidea Fw TGACATTCATGGGATTGCAGAC
m_Cidea Rv GGCCAGTTGTGATGACTAAGAC
m_Cox7a1 Fw GCTCTGGTCCGGTCTTTTAGC
m_Cox7a1 Rv GTACTGGGAGGTCATTGTCGG
m_ Cpt1a Fw CTCCGCCTGAGCCATGAAG
m_ Cpt1a Rv CACCAGTGATGATGCCATTCT
m_Cpt1b Fw GCACACCAGGCAGTAGCTTT
m_Cpt1b Rv CAGGAGTTGATTCCAGACAGGTA
m_Cpt2 Fw CAGCACAGCATCGTACCCA
m_Cpt2 Rv TCCCAATGCCGTTCTCAAAAT
m_Cxcl14 Fw GAAGATGGTTATCGTCACCACC
m_Cxcl14 Rv CGTTCCAGGCATTGTACCACT
m_Gapdh Fw TGAAGCAGGCATCTGAGGG
m_Gapdh Rv CGAAGGTGGAAGAGTGGGA
m_Il1 Fw GCAACTGTTCCTGAACTCAACT
m_Il1 Rv ATCTTTTGGGGTCCGTCAACT
m_Il-4Fw GGTCTCAACCCCCAGCTAGT
m_Il-4Rv GCCGATGATCTCTCTCAAGTG
m_Prdm16 Fw CCACCAGCGAGGACTTCAC
m_Prdm16 Rv GGAGGACTCTCGTAGCTCGAA
m_Tnfa Fw CCCTCACACTCAGATCATCTTCT
m_Tnfa Rv GCTACGACGTGGGCTACAG
m_Ucp1 Fw GTGAACCCGACAACTTCCGAA
m_Ucp1 Rv TGAAACTCCGGCTGAGAAGAT

Tissue processing and flow cytometry

For the isolation of BAT SVF and adipocytes fractions, mice were perfused with 20 ml PBS, and BAT was collected, dissociated, and digested with 1 mg/mL liberase TL and 2 U/mL DNAse for 30 min at 37 °C with shaking. The cell suspension was then passed through a 70-µm strainer and centrifuged at 1500 rpm. The part that was retained by the filter was considered the adipocyte fraction whereas the one that passes was the stromal vascular fraction (SVF). For flow cytometry, pelleted erythrocytes were lysed with a red-cell lysis buffer (NH_4Cl, $NaHCO_3$, 20 mM EDTA), and leukocytes were subsequently resuspended in flow cytometry buffer (PBS containing 1% FBS and 5 mM EDTA). Single-cell suspensions were stained with the following surface-marker antibodies: rat anti-mouse CD45 V450 (Clone 30-F11), rat anti-mouse CD11b Brilliant Violet (BV) 785 (Clone M1/70) and rat anti-mouse F4/80 APC-Cyanine 7(Clone BM8). Dead cells were excluded by (4',6-diamidino-2-fenilindol) DAPI staining. Flow cytometry experiments were performed in a BD LSRFortessa cell analyzer, and data were analyzed with FlowJo software.

Cell culture

Primary brown preadipocytes from WT and MCJ^{KO} mice were differentiated to brown adipocytes in 10% fetal bovine serum (FBS) medium supplemented with 20 nM insulin, 1 nM T3, 125 µM indomethacin, 2 µg/ml dexamethasone, and 50 mM IBMX for 48 h and maintained with 20 nM of insulin and 1 nM of T3 for 8 days. The day prior the experiment, 100 µM palmitate is added overnight.

Immortalized brown preadipocytes (BAT1 cells) were cultured in BAT1 media (DMEM/F12 media with 10% FBS and 1% penicillin/streptomycin) and after 24 BAT1 media is supplemented with 500 µM IBMX (3-isobutyl-1-methylxanthine), 5 µM dexamethasone, 1 µM rosiglitazone, 20 nM insulin and 1 nM triiodothyronine (T3). After 3 days, media was replaced with maintenance media supplementing BAT1 media with 20 nM insulin and 1 nM T3. Experiments were conducted three days after adding maintenance media. The day prior the experiment, 100 µM palmitate was added overnight[56].

Cell transfection

Cell transfection was performed using the Lipofectamine™ 3000 Reagent Protocol. Briefly, after plating the cells, the DNA was diluted in Opti-MEM™ Medium, and P3000™ Reagent. The siRNA (10 µM) was mixed with the Lipofectamine™ 3000 Reagent (1:1 ratio). Finally, the mixture was added to the cells and incubated for 48 h.

Adipocyte respirometry measurements

Brown pre-adipocytes were plated and differentiated in gelatin (0.1%) coated 96 Seahorse XF cell culture plates following the protocol described above. 16 h before the assay, the cell medium was changed to substrate-limited medium (SLM). For MitoStress, SML was composed by DMEM supplemented with 1% fatty acid free BSA, 2 mM glutamine, 100 µg ml^{-1} penicillin/streptomycin and 1% FBS. For FAO assay we followed Seahorse XF Palmitate-BSA FAO Substrate Guide where SML was composed by DMEN supplemented with 0.5 mM glucose, 1 mM glutamine, 0.5 mM L-carnitine hydrochloride, 100 µg ml−1 penicillin/streptomycin and 1% FBS. MitoStress test was performed in XF medium containing 25 mM glucose, 2 mM L-glutamine, and 1 mM sodium pyruvate using an XF-96 extracellular flux analyzer (Agilent). For the FAO assay, 1 mM palmitate conjugated to 0.17 mM BSA or a 0.17 mM BSA was added to the XF medium containing 2.5 mM glucose, 0.5 mM L-carnitine hydrochloride, and 5 mM HEPES. Cells were stimulated with the following drugs: isoproterenol (ISO) for mitostress test, followed in both tests by oligomycin, FCCP, and antimycin A plus rotenone (all at a final concentration of 1 µM). The protocol for all the drugs followed a 3 min mix, 2 min wait, and a 3 min measure cycle that was repeated 3 times. After the analysis, data were normalized to protein levels assessed by Bradford quantification. Basal respiration (OCR basal−OCR nonmitochondrial), oxygen consumption in response to ISO (OCR ISO−OCR basal), maximal respiration (OCR FCCP − non-mitochondrial respiration), ATP production (OCR ISO − OCR oligomycin) and proton leak (OCR oligomycin − OCR non-mitochondrial) were calculated[9].

Mitochondria isolation

Mitochondria were isolated from BAT by suspending BAT in a sucrose buffer in a 2 mL glass Potter-Elvehjem tube and homogenized by up and down strokes with a motor-driven Teflon pestle. The homogenate was centrifuged at 1000 × *g* 5 min at 4 °C and the supernatant was centrifuged 12,000 × *g* 3 min at 4 °C twice until the pellet was yielded the mitochondria-containing fraction[57].

Mitochondrial DNA/genomic DNA ratio

BAT tissue was homogeneized in PBS, and the pellet was lysed in TNES buffer (50 mM Tris pH 7.4, 100 mM EDTA pH 8,0, 400 mM NaCl, 0.5% SDS) supplemented with proteinase K (20 mg/ml) overnight at 55 °C. The reaction was stopped by addition of 6 M NaCl, and samples were centrifuged for 5 min at 13,000 g. DNA in supernatants was precipitated with 100% ethanol and washed with 70% ethanol. After drying, the DNA was resuspended in DNase free water, quantified, and analyzed by RT-PCR. Mitochondrial DNA was detected with primers for 16S rRNA and nuclear DNA was detected with primers for HK2[58]. Primers and Taqman probe are listed below:

m_Hk2 Fw TGATCGCCTGCTTATTCACGG
m_Hk2 Rv AACCGCCTAGAAATCTCCAGA
m_16s Fw CCGCAAGGGAAAGATGAAAGAC
m_16s Rv TCGTTTGGTTTCGGGGTTTC

Transmission electron microscopy

Electron microscopy analysis was performed at the Electron Microscopy Unit of the Spanish National Center for Biotechnology (CNB-CSIC). BAT samples were harvested from HFD-fed mice for 12 weeks. Tissue fragments (1–2 mm^3) were fixed in 2.5% glutaraldehyde/4% paraformaldehyde in PBS for 4 h at room temperature, followed by overnight incubation at 4 °C. After PBS washes, samples were postfixed for 1 h at 4 °C in a solution with 1% osmium tetroxide and 0.8% potassium ferricyanide. Samples were rinsed in distilled H_2O and treated with 2% uranyl acetate for 1 h at 4 °C. Tissues were dehydrated through a graded acetone series (30–100%) at 4 °C, embedded in epoxy resin (Epon 812, Sigma) and polymerized at 60 °C for 48 h. Ultrathin sections (70 nm) were obtained by Leica EM UC6 ultramicrotome, mounted on formvar/carbon coated grids and stained with uranyl acetate and lead citrate following conventional protocols. Samples were examined on a JEOL JEM 1011 (100 kV) transmission electron microscope. Micrographs were obtained with a Gatan Erlangshen ES1000W CCD camera at various magnifications. Mean area, perimeter, aspect ratio, circularity and cristae density were estimated using ImageJ software.

Quantification of mitochondrial superoxide formation in isolated mitochondria: mitoSOX + HPLC

Mitochondrial oxidative stress and superoxide was also measured by an HPLC-based method to quantify triphenylphosphonium-linked 2-hydroxyethidium (2-OH–mito-E +)[59]. BAT was homogenized in Hepes buffer (50 mM Hepes, 70 mM sucrose, 220 mM mannitol, 1 mM EGTA, and 0.033 mM bovine serum albumin) and centrifuged at 1500 × *g* (10 min at 4 °C) and 2000 × *g* for 5 min. The supernatant was then centrifuged at 20,000 × *g* for 20 min, and the pellet was resuspended in 1 ml of Hepes buffer. The latter step was repeated, and the pellet was resuspended in 1 ml of tris buffer (10 mM tris, 340 mM sucrose, 100 mM KCl, and 1 mM EDTA). Mitochondrial suspensions were diluted to a final protein concentration of 0.1 mg/ml in 0.5 ml of PBS buffer containing mitoSOX (5 µM) and incubated for 15 min at 37 °C. After the incubation step, water:acetonitrile (1:1) was added, samples were centrifuged, and 100 µl of the supernatant was subjected to HPLC analysis. The system consisted of a control unit, two pumps, mixer, detectors, column oven, degasser, and an autosampler (AS-2057 plus with 4 °C cooling device) from Jasco (Groß-Umstadt, Germany) and a C18- Nucleosil 100-3 (125 × 4) column from Macherey & Nagel (Düren, Germany). A high-pressure gradient was used with acetonitrile and 50 mM citrate buffer (pH 2.2) as mobile phases with the following percentages of the organic solvent: 0 min, 24%; 9–10 min, 24–53%; 10–25.5 min, 53–72%; 25.5–26 min, 72–95%; 26–30 min, 95%; 30–31 min, 95–24%; and 31–40 min, 24%. The flow was 0.55 ml/min, and mitoSOX was detected by its absorption at 360 nm, whereas 2-OH–mito-E+ and mito-E+ were detected by fluorescence (excitation at 500 nm/emission at 580 nm). The 2-OH–mito-E+ and mito-E+ standards were synthesized by the Fremy's salt and chloranil method as described (77). To suppress mitochondrial ROS formation, especially superoxide, selected samples were coincubated with the cell-permeable superoxide dismutase mimetic and peroxynitrite scavenger manganese (III) tetrakis (4-benzoic acid) porphyrin chloride (10 µM) or the mitochondria-targeted scavenger of ROS (2-(2,2,6,6-tetramethylpiperidin-1-oxyl-4-ylamino)-2-oxoethyl) triphenylphosphonium chloride (10 µM).

Proteomics

BAT tissue (100 µg per sample) and isolated BAT mitochondria (20 µg per sample) from HFD-fed mice were homogenized with a FastPrep-24 5 G system (MP Biomedicals). Total protein was digested according to the filter aided sample preparation (FASP) protocol[60]. The dried peptides were dissolved in 150 mM triethylammonium bicarbonate (TEAB) buffer. Equal amounts of each peptide sample were labeled using the 18-plex tandem mass tag (TMTp) kit (Thermo Scientific). Labeled peptides were separated by liquid chromatography and analyzed by tandem mass spectrometry (LC-MS/MS) using a C-18 reversed phase EASY nano-column (75 µm I.D. x 50 cm, 2 µm particle size, Acclaim PepMap RSLC, 100 C18; Thermo Scientific) in a continuous gradient consisting of 0–30% B for 360 min and 50–90% B for 3 min (A = 0.5% formic acid; B = 90% acetonitrile, 0.5% formic acid). Peptides were eluted from the reverse-phase nano-column to an emitter nanospray needle for real-time ionization and peptide fragmentation on an Orbitrap Trybrid Fusion mass spectrometer (Thermo Fisher). An enhanced Fourier transform-resolution spectrum (resolution = 60,000) followed by the MS/MS spectra from the 15 most intense parent ions was performed. All spectra were analyzed with Proteome Discoverer (version 2.5, Thermo Fisher Scientific) using SEQUEST-HT (Thermo Fisher Scientific). Data were searched against a mouse Uniprot database (June 2022), and peptide identification was performed with a false discovery rate (FDR) ≤ 1%[61]. Protein quantification and statistical analysis were performed based on the weighted spectrum, peptide and protein (WSPP) statistical model using the iSanXoT package[61,62]. Differences in peptide and protein abundance or functional behavior were estimated based on the comparison of the groups' Zq, or Zc medians, respectively, as determined by the WSPP statistical model. Proteins or functional changes were considered statistically significant with a p value < 0.05 based on a two-sided t test comparison of the Z values using limma[63]. Protein changes were considered statistically significant with $p < 0.05$. Proteins were annotated using the Ingenuity Knowledge Database (Ingenuity Pathway Analysis, IPA) and R studio. The mass spectrometry proteomics data have been deposited to the ProteomeXchange Consortium repository with the dataset identifier PXD057026.

Metabolite isolation

BAT was flash frozen and powderized with a mortar and pestle in a liquid nitrogen bath. Approximately 10 mg of powder was transferred into tubes and re-suspended in 800 uL ice-cold LC-MS grade 60:40 methanol:Water (ThermoFisher). Samples were vortexed for 10 min at 4 °C. Then, 500 µL of ice-cold LC-MS grade chloroform (ThermoFisher) was added to the lysate and samples were vortexed for an additional 10 min at 4 °C. Samples were centrifuged at 16,000 × *g* for 10 min at 4 °C, creating a polar layer on top, a non-polar layer on the bottom, and a protein layer at the interface. The top layer was transferred to a new tube, dried down in a speedvac to be used for LCMS analysis. The non-polar layer was discarded. The protein layer was lysed in RIPA buffer (150 mM NaCl, 50 mM Tris HCl pH 7.5, 0.1% SDS, 1% Triton-X 100 (Sigma), 0.5% deoxycholate (Sigma), complete EDTA-free protease inhibitor (Sigma). Protein in each sample was quantified using the Pierce BCA Protein Assay Kit (Life Technologies). Protein concentrations were used for normalization of sample inputs prior to LC-MS analysis.

Liquid chromatography mass spectrometry

A Qexactive Plus quadrupole orbitrap mass spectrometer (Thermo Fisher Scientific) equipped with an Ion Max source and a HESI II probe coupled to a Vanquish Horizon UHPLC System (Thermo Fisher Scientific) was used to perform LC-MS experiments. Prior to operation, the instrument underwent mass calibration for positive and negative ion mode using Calmix (Thermo Fisher Scientific) every 7 days. Dried samples were re-suspended in enough HPLC-grade water to have a final concentration of 1 ug protein per mL water. 2 µL of the re-suspended polar metabolite samples were injected onto a SeQuant ZIC-pHILIC 5 µm 150 × 2.1 mm analytical column equipped with a 2.1 × 20 mm guard column (MilliporeSigma). The column oven was held at 25 °C and the autosampler tray was held at 4 °C. Buffer A was comprised of 20 mM ammonium carbonate, 0.1% ammonium hydroxide. Buffer B was comprised of 100% acetonitrile. The

chromatographic gradient was run at a flow rate of 0.150 mL/min as follows: 0-20 min: linear gradient from 80 to 20% B; 20–20.5 min: linear gradient from 20 to 80% B; 20.5–28 min: hold at 80% B. The mass spectrometer was operated in full-scan, polarity switching mode, with the spray voltage set to 4.0 kV, the heated capillary at 350 °C, and the HESI probe at 350 °C. The sheath gas flow was 10 units, the auxiliary gas flow was 2 units, and the sweep gas flow was 1 unit. MS data was collected in a range of m/z = 70–1000. The resolution set at 70,000, the AGC target at 1×10^6, and the maximum injection time at 20 msec. Differentially encountered metabolites ($p < 0.05$) were analyzed by Metabolite Set Enrichment Analysis (MSEA) using Metaboanalyst 5.0.

Polar metabolomics

BAT1 cells were washed twice and supplemented with DMEM with 1 mM sodium pyruvate and 25 mM ^{13}C-glucose. After 4 h, cells were washed and incubated with 80:20% methanol:water solution at −80 °C for 15 min. Extracts were centrifuged (10 min at 18,000 × *g*) and supernatants were dried down. Samples were submitted to the Metabolomics Core at the Beth Israel Deaconess Medical Center for further polar metabolite detection by QTRAP® 5500 System and Reverse-Phase Ion-Pairing Chromatography. Differentially encountered metabolites ($p < 0.05$) were analyzed by Metabolite Set Enrichment Analysis (MSEA) using Metaboanalyst 5.0.

Statistics & reproducibility

The data are expressed as means ± SEM. Two-group comparisons were analyzed by two-tailed Student t test, and multiple group comparisons were analyzed by one-way or two-way analysis of variance coupled with the Tukey's or Sidak's multigroup test, respectively. Pearson correlation analysis was performed to study correlation between variables. To ensure that changes in EE were independent of the weight of the mice, EE (Kcal/h) was also analyzed via ANCOVA as reported[64]. For all tests, differences were considered significant at a two-sided $p < 0.05$. To choose the size of the sample we have used the 3 R rule to ensure statistical validity and significance with the chosen size. Biostatisticians help in designing our animal experiments using most updated statistical methods to ensure that the correct number of animals will be employed in each experiment. The number of animals in each group is determined by the statistical power that is required to detect significant biologically relevant differences. A meaningful difference in means at least 80% power for one- and two-sided testing. Animals that presented disease or had been bitten because fight in the cage were excluded. Animals were randomized into groups. Technicians were blinded analyzing samples and most of the studies were performed in such condition, except in some experiments where samples were needed to be loaded correctly. All displayed points represented biological replicates. All analyses were performed using Excel (Microsoft Corp.), R studio and GraphPad PRISM 8 software. The statistics details for all the experiments were indicated in the figure legends.

Reporting summary

Further information on research design is available in the Nature Portfolio Reporting Summary linked to this article.

Data availability

All data generated or analyzed during this study are included in this published article (and its supplementary information files). The mass spectrometry proteomics data have been deposited to the ProteomeXchange Consortium repository with the dataset identifier PXD057026. The mass spec-based metabolomics have been deposited to the EMBL-EBI MetaboLights database with the identifier MTBLS11505[65]. Any further information is available from the corresponding authors. Source data are provided with this paper.

References

1. Upadhyay, J., Farr, O., Perakakis, N., Ghaly, W. & Mantzoros, C. Obesity as a disease. *Med. Clin. North Am.* **102**, 13–33 (2018).
2. Nikolic, I., Leiva, M. & Sabio, G. The role of stress kinases in metabolic disease. *Nat. Rev. Endocrinol.* **16**, 697–716 (2020).
3. Friedman, J. 20 years of leptin: leptin at 20: An overview. *J. Endocrinol.* **223**, T1–T8 (2014).
4. Giralt, M., Cereijo, R. & Villarroya, F. Adipokines and the endocrine role of adipose tissues. *Handb. Exp. Pharm.* **233**, 265–282 (2016).
5. Valencak, T. G., Osterrieder, A. & Schulz, T. J. Sex matters: The effects of biological sex on adipose tissue biology and energy metabolism. *Redox Biol.* **12**, 806–813 (2017).
6. Stern, J. H., Rutkowski, J. M. & Scherer, P. E. Adiponectin, leptin, and fatty acids in the maintenance of metabolic homeostasis through adipose tissue crosstalk. *Cell Metab.* **23**, 770–784 (2016).
7. Sabio, G. et al. A stress signaling pathway in adipose tissue regulates hepatic insulin resistance. *Science* **322**, 1539–1543 (2008).
8. Manieri, E. et al. Adiponectin accounts for gender differences in hepatocellular carcinoma incidence. *J. Exp. Med* **216**, 1108–1119 (2019).
9. Matesanz, N. et al. p38alpha blocks brown adipose tissue thermogenesis through p38delta inhibition. *PLoS Biol.* **16**, e2004455 (2018).
10. Matesanz N, B. E. et al. MKK6 controls T3-mediated browning of white adipose tissue. *Nat. Commun.* **8**, 1–14 (2017).
11. Wang, W. & Seale, P. Control of brown and beige fat development. *Nat. Rev. Mol. Cell Biol.* **17**, 691–702 (2016).
12. Cannon, B. & Nedergaard, J. Brown adipose tissue: function and physiological significance. *Physiol. Rev.* **84**, 277–359 (2004).
13. Ikeda, K. et al. UCP1-independent signaling involving SERCA2b-mediated calcium cycling regulates beige fat thermogenesis and systemic glucose homeostasis. *Nat. Med* **23**, 1454–1465 (2017).
14. Roesler, A. & Kazak, L. UCP1-independent thermogenesis. *Biochem J.* **477**, 709–725 (2020).
15. Cannon, B. & Nedergaard, J. Nonshivering thermogenesis and its adequate measurement in metabolic studies. *J. Exp. Biol.* **214**, 242–253 (2011).
16. Lowell, B. B. & Shulman, G. I. Mitochondrial dysfunction and type 2 diabetes. *Science* **307**, 384–387 (2005).
17. Patti, M. E. & Corvera, S. The role of mitochondria in the pathogenesis of type 2 diabetes. *Endocr. Rev.* **31**, 364–395 (2010).
18. Jang, J. Y., Blum, A., Liu, J. & Finkel, T. The role of mitochondria in aging. *J. Clin. Investig.* **128**, 3662–3670 (2018).
19. Hatle, K. M. et al. MCJ/DnaJC15, an endogenous mitochondrial repressor of the respiratory chain that controls metabolic alterations. *Mol. Cell Biol.* **33**, 2302–2314 (2013).
20. Iruzubieta, P. et al. Boosting mitochondria activity by silencing MCJ overcomes cholestasis-induced liver injury. *JHEP Rep.* **3**, 100276 (2021).
21. Goikoetxea-Usandizaga, N. et al. The outcome of boosting mitochondrial activity in alcohol-associated liver disease is organ-dependent. *Hepatology* **78**, 878–895 (2023).
22. Whittle, A. J. et al. BMP8B increases brown adipose tissue thermogenesis through both central and peripheral actions. *Cell* **149**, 871–885 (2012).
23. van Marken Lichtenbelt, W. D. et al. Cold-activated brown adipose tissue in healthy men. *N. Engl. J. Med.* **360**, 1500–1508 (2009).
24. Nedergaard, J., Bengtsson, T. & Cannon, B. Unexpected evidence for active brown adipose tissue in adult humans. *Am. J. Physiol. Endocrinol. Metab.* **293**, E444–E452 (2007).
25. Bates, R., Huang, W. & Cao, L. Adipose tissue: An emerging target for adeno-associated viral vectors. *Mol. Ther. Methods Clin. Dev.* **19**, 236–249 (2020).
26. Liu, X. et al. Brown adipose tissue transplantation improves whole-body energy metabolism. *Cell Res.* **23**, 851–854 (2013).

27. Villarroya, F. & Giralt, M. The beneficial effects of brown fat transplantation: Further evidence of an endocrine role of brown adipose tissue. *Endocrinology* **156**, 2368–2370 (2015).
28. Zhu, Z. et al. Enhanced sympathetic activity in mice with brown adipose tissue transplantation (transBATation). *Physiol. Behav.* **125**, 21–29 (2014).
29. Chang, J. S. Recent insights into the molecular mechanisms of simultaneous fatty acid oxidation and synthesis in brown adipocytes. *Front Endocrinol. (Lausanne)* **14**, 1106544 (2023).
30. Cero, C. et al. beta3-Adrenergic receptors regulate human brown/beige adipocyte lipolysis and thermogenesis. *JCI Insight* **6**, 1–20 (2021).
31. Wikstrom, J. D. et al. Hormone-induced mitochondrial fission is utilized by brown adipocytes as an amplification pathway for energy expenditure. *EMBO J.* **33**, 418–436 (2014).
32. Lettieri-Barbato, D. Redox control of non-shivering thermogenesis. *Mol. Metab.* **25**, 11–19 (2019).
33. Chondronikola, M. et al. Brown Adipose Tissue Activation Is Linked to Distinct Systemic Effects on Lipid Metabolism in Humans. *Cell Metab.* **23**, 1200–1206 (2016).
34. Yoneshiro, T. et al. BCAA catabolism in brown fat controls energy homeostasis through SLC25A44. *Nature* **572**, 614–619 (2019).
35. Wek, R. C. Role of eIF2alpha kinases in translational control and adaptation to cellular stress. *Cold Spring Harb. Perspect Biol.* **10**, 1–16 (2018).
36. Paulo, E. et al. Brown adipocyte ATF4 activation improves thermoregulation and systemic metabolism. *Cell Rep.* **36**, 109742 (2021).
37. Wallimann, T., Tokarska-Schlattner, M., Kay, L. & Schlattner, U. Role of creatine and creatine kinase in UCP1-independent adipocyte thermogenesis. *Am. J. Physiol. Endocrinol. Metab.* **319**, E944–E946 (2020).
38. Veliova, M. et al. Blocking mitochondrial pyruvate import in brown adipocytes induces energy wasting via lipid cycling. *EMBO Rep.* **21**, e49634 (2020).
39. Bartelt, A. & Widenmaier, S. B. Proteostasis in thermogenesis and obesity. *Biol. Chem.* **401**, 1019–1030 (2020).
40. Bartelt, A. et al. Brown adipose tissue thermogenic adaptation requires Nrf1-mediated proteasomal activity. *Nat. Med* **24**, 292–303 (2018).
41. Park, E. J. et al. Ssu72 phosphatase is essential for thermogenic adaptation by regulating cytosolic translation. *Nat. Commun.* **14**, 1097 (2023).
42. Enerback, S. et al. Mice lacking mitochondrial uncoupling protein are cold-sensitive but not obese. *Nature* **387**, 90–94 (1997).
43. Cicuendez, B., Perez-Garcia, J. & Folgueira, C. A combination of a dopamine receptor 2 agonist and a kappa opioid receptor antagonist synergistically reduces weight in diet-induced obese rodents. *Nutrients* **16**, 1–13 (2024).
44. Folgueira, C. et al. Oral pharmacological activation of hypothalamic guanylate cyclase 2C receptor stimulates brown fat thermogenesis to reduce body weight. *Neuroendocrinology* **110**, 1042–1054 (2020).
45. Folgueira, C. et al. Uroguanylin action in the brain reduces weight gain in obese mice via different efferent autonomic pathways. *Diabetes* **65**, 421–432 (2016).
46. Cruz, F. M. et al. Exercise triggers ARVC phenotype in mice expressing a disease-causing mutated version of human plakophilin-2. *J. Am. Coll. Cardiol.* **65**, 1438–1450 (2015).
47. Folgueira, C. et al. Hypothalamic dopamine signaling regulates brown fat thermogenesis. *Nat. Metab.* **1**, 811–829 (2019).
48. Canhoto, A. J., Chestukhin, A., Litovchick, L. & DeCaprio, J. A. Phosphorylation of the retinoblastoma-related protein p130 in growth-arrested cells. *Oncogene* **19**, 5116–5122 (2000).
49. Liu, X. et al. Brown adipose tissue transplantation reverses obesity in Ob/Ob mice. *Endocrinology* **156**, 2461–2469 (2015).
50. Sabio, G. et al. Prevention of steatosis by hepatic JNK1. *Cell Metab.* **10**, 491–498 (2009).
51. Saenz de Urturi, D. et al. Methionine adenosyltransferase 1a antisense oligonucleotides activate the liver-brown adipose tissue axis preventing obesity and associated hepatosteatosis. *Nat. Commun.* **13**, 1096 (2022).
52. Huynh, F. K., Green, M. F., Koves, T. R. & Hirschey, M. D. Measurement of fatty acid oxidation rates in animal tissues and cell lines. *Methods Enzymol.* **542**, 391–405 (2014).
53. Gonzalez-Teran, B. et al. Eukaryotic elongation factor 2 controls TNF-alpha translation in LPS-induced hepatitis. *J. Clin. Invest* **123**, 164–178 (2013).
54. Morant-Ferrando, B. et al. Fatty acid oxidation organizes mitochondrial supercomplexes to sustain astrocytic ROS and cognition. *Nat. Metab.* **5**, 1290–1302 (2023).
55. Katz, J., Rognstad, R. & Kemp, R. G. Isotope discrimination effects in the metabolism of tritiated glucose. *J. Biol. Chem.* **240**, PC1484–PC1486 (1965).
56. Latorre-Muro, P. et al. A cold-stress-inducible PERK/OGT axis controls TOM70-assisted mitochondrial protein import and cristae formation. *Cell Metab.* **33**, 598–614.e597 (2021).
57. Calvo, E. et al. Functional role of respiratory supercomplexes in mice: SCAF1 relevance and segmentation of the Q(pool). *Sci. Adv.* **6**, eaba7509 (2020).
58. Quiros, P. M., Goyal, A., Jha, P. & Auwerx, J. Analysis of mtDNA/nDNA ratio in mice. *Curr. Protoc. Mouse Biol.* **7**, 47–54 (2017).
59. Santamans, A. M. et al. MCJ: A mitochondrial target for cardiac intervention in pulmonary hypertension. *Sci. Adv.* **10**, eadk6524 (2024).
60. Cardona, M. et al. Executioner caspase-3 and 7 deficiency reduces myocyte number in the developing mouse heart. *PLoS One* **10**, e0131411 (2015).
61. Navarro, P. et al. General statistical framework for quantitative proteomics by stable isotope labeling. *J. Proteome Res.* **13**, 1234–1247 (2014).
62. Rodriguez, J. M. et al. iSanXoT: A standalone application for the integrative analysis of mass spectrometry-based quantitative proteomics data. *Comput Struct. Biotechnol. J.* **23**, 452–459 (2024).
63. Ritchie, M. E. et al. limma powers differential expression analyses for RNA-sequencing and microarray studies. *Nucleic Acids Res.* **43**, e47 (2015).
64. Muller, T. D., Klingenspor, M. & Tschop, M. H. Revisiting energy expenditure: how to correct mouse metabolic rate for body mass. *Nat. Metab.* **3**, 1134–1136 (2021).
65. Yurekten, O. et al. MetaboLights: Open data repository for metabolomics. *Nucleic Acids Res.* **52**, D640–D646 (2024).

Acknowledgements

We thank Electron Microscopy Facility (Centro Nacional de Biotecnología, CSIC) for preparing samples (Epon embedding), obtaining the ultrathin sections and TEM visualization. The project that gave rise to these results received the support of a fellowship from" la Caixa" Foundation (ID 100010434). The fellowship code is LCF/BQ/DR21/11880010 to B.C. C.F was funded with Sara Borrell (CD19/ 00078), NNF23SA0083952-EASO/Novo Nordisk New Investigator Award in Basic Sciences 2023, EFSD/Lilly Young Investigator Award 2022, Society for Endocrinology/Early Career Grant 2022, FSEEN/ Jóvenes endocrinólogos 2022, EFSD/Novo Nordisk Rising Star 2024, IBSA Foundation Fellowship Endocrinology 2023. This work has been supported by the following projects: PMP21/00057 funded by the Instituto de Salud Carlos III (ISCIII) - European Union (FEDER/FSE) "Una manera de hacer Europa"/ "El FSE invierte en tu futuro"/ Next Generation EU and

cofunded by the European Union / Plan de Recuperación, Transformación y Resiliencia (PRTR); PID2022-138525OB-I00 de la Agencia Estatal de Investigación 10.13039/501100011033, financiado por MICIU/AEI/10.13039/501100011033 fondos FEDER and EU, PDC2021-121147-I00 and PID2019-104399RB-I00 funded by MCIN/AEI/10.13039/501100011033 and the European Union "NextGenerationEU"/Plan de Recuperación Transformación y Resiliencia -PRTR; Grant RED2022-134397-T funded by MCIN/AEI/10.13039/501100011033 and, as appropriate, by "ERDF A way of making Europe", by the "European Union" or by the "European Union NextGenerationEU/PRTR"; Fundación Jesús Serra; EFSD/Lilly Dr Sabio; 2017 Leonardo Grant BBVA Foundation (Investigadores-BBVA-2017); Comunidad de Madrid IMMUNOTHERCAN-CM S2010/BMD-2326 and B2017/BMD-373; Fundación AECC PROYE19047SABI. PreMed-Exp: PMP21/00057, PMP21/00113 Infraestructura de Medicina de Precisión asociada a la Ciencia y Tecnología IMPACT-2021, Instituto de Salud Carlos III (GS, JLT). The project leading to these results has received funding from the" la Caixa" Foundation under the project code "HR24-00581" (G.S). G.S is a Miembro Numerario of the RACVE. J.P-G was supported by the fellowship from" la Caixa" Foundation (ID 100010434), the fellowship code is LCF/BQ/DR24/12080018. A.C was supported by the European Union's Horizon 2020 research and innovation program under the Marie Skłodowska-Curie grant agreement n. 713,673 and by Becas de doctorado INPhINIT "la Caixa" 2018. PLM acknowledges NIH NIDDK grant K99DK133502. M.M is supported by Instituto de Salud Carlos III (ISCIII) and the European Union project PI20/00743. P.A is supported by MCIU/AEI/FEDER, UE (PID2021-124425OB-I00) and Basque Government, Department of Education (IT1476-22) and PMP21/00080 de Medicina de Precisión asociada a la Ciencia y Tecnología IMPACT-2021, Instituto de Salud Carlos III. J.P.B is funded by MICIU/AEI (PID2022-138813OB-I00), la Caixa Foundation (grant agreement LCF/PR/HR23/52430016), Instituto de Salud Carlos III (CB16/10/00282) and the European Union's Horizon Europe research and innovation program under the MSCA Doctoral Networks 2021 (101072759; FuEl ThEbRaiN In healtThY aging and age-related diseases, ETERNITY), AEI grants PID2019-105699RB-I00, PID2022-138813OB-I00 and PDC2021-121013-I00; HORIZON-MSCA-2021-DN-01grant 101072759; and La Caixa Research Health grant HR23-00793. PP acknowledges NIH grant R01DK136640. JAE was supported by competitive grants: PID2021-127988OB-I00 funded by MCIN/AEI/10.13039/501100011033/ FEDER, UE; Human Frontier Science Program (grant RGP0016/2018), Leducq Transatlantic Networks (17CVD04) and CIBERFES [CB16/10/00282], Centro de Investigación Biomédica. Instituto de Salud Carlos III.The CNIO and CNIC are supported by the Instituto de Salud Carlos III (ISCIII), the Ministerio de Ciencia e Innovación (MCIN) and the Pro CNIC Foundation) and is a Severo Ochoa Center of Excellence (grant CEX2020-001041-S funded by MICIN/AEI/10.13039/501100011033).

Author contributions

G.S, C.F conceptualized the project and generated project resources. G.S, B.C, C.F designed the study and developed the hypothesis. B.C, C.F performed the experiments, analyzed the data and prepared figures. A.M, J.A.L, A.C, J.P-G, B.P, D. J-B, P.-LM, P.V, M.J (Madison Jerome), B.G-S, R. R-B, M.L (Magdalena Leiva), E.R, M. L (Marta León), L.L-V, N.G, A.D assisted in experiments analysis. L. H-C, J. L-T, M.M, provided human samples. P.A (Pablo Aguiar), M.J (Martin Jastroch), P.A (Patricia Aspichueta), J.B.S, P.P, J.A.E, J.P.B, J.V provided expertise and critical feedback. G.S, C.F, B.C wrote the manuscript with input from all authors.

Competing interests

The authors declare no competing interests.

Additional information

Supplementary information The online version contains supplementary material available at https://doi.org/10.1038/s41467-024-54353-4.

Correspondence and requests for materials should be addressed to Cintia Folgueira or Guadalupe Sabio.

Peer review information *Nature Communications* thanks Paul Yen, and the other, anonymous, reviewer(s) for their contribution to the peer review of this work. A peer review file is available.

[1]Centro Nacional de Investigaciones Cardiovasculares (CNIC), Madrid, Spain. [2]Organ Crosstalk in Metabolic Diseases Group, Molecular Oncology Program, Spanish National Cancer Centre (CNIO), Madrid, Spain. [3]CIBER de Enfermedades Cardiovasculares (CIBERCV), Instituto de Salud Carlos III, Madrid, Spain. [4]Centro de Investigación Biomédica en Red sobre Fragilidad y Envejecimiento Saludable (CIBERFES), Instituto de Salud Carlos III, Madrid, Spain. [5]Department of Physiology, CIMUS, University of Santiago de Compostela, Santiago de Compostela, Spain. [6]CIBER Fisiopatología de la Obesidad y Nutrición (CIBERobn), Instituto de Salud Carlos III, Madrid, Spain. [7]Institute of Functional Biology and Genomics, University of Salamanca, CSIC, Salamanca, Spain. [8]Institute of Biomedical Research of Salamanca, University Hospital of Salamanca, University of Salamanca, CSIC, Salamanca, Spain. [9]Department of Cancer Biology, Dana-Farber Cancer Institute, Boston, MA, USA. [10]Department of Cell Biology, Harvard Medical School, Boston, MA, USA. [11]Program in Molecular Medicine, UMass Chan Medical School, Worcester, MA, USA. [12]Department of Physiology, Faculty of Medicine and Nursing, University of the Basque Country UPV/EHU. Leioa, Biobizkaia Health Research Institute, Barakaldo, Spain. [13]Department of Immunology, School of Medicine, Universidad Complutense de Madrid, Madrid, Spain. [14]Molecular Imaging Biomarkers and Theragnosis Lab, Center for Research in Molecular Medicine and Chronic Diseases (CiMUS). University of Santiago de Compostela (USC), Santiago de Compostela, Spain. [15]Molecular Imaging Group, Health Research Institute of Santiago de Compostela (IDIS), Santiago de

Compostela, Spain. [16]Nuclear Medicine Service, University Clinical Hospital of Santiago de Compostela (CHUS), Santiago de Compostela, Spain. [17]Complejo Asistencial de Zamora, Zamora, Spain. [18]Bariatric Surgery Unit. Department of General Surgery, University Hospital of Salamanca. Department of Surgery. University of Salamanca, Salamanca, Spain. [19]Department of Internal Medicine, University Hospital of Salamanca-IBSAL, Salamanca, Spain. [20]Department of Medicine. University of Salamanca, Salamanca, Spain. [21]Department of Molecular Biosciences, The Wenner-Gren Institute, Stockholm University, Stockholm, Sweden. [22]Department of Cardiology 1, University Medical Center Mainz, Mainz, Germany. [23]German Center for Cardiovascular Research (DZHK), Partner Site Rhine-Main, Mainz, Germany. [24]Centro de Investigación Biomédica en Red sobre enfermedades hepáticas y digestivas (CIBERehd), Instituto de Salud Carlos III, Madrid, Spain. [25]UMass Chan Medical School Cancer Center, Worcester, MA, USA. ✉e-mail: cintia.folgueira@cnic.es; gsabio@cnio.es